Supplementary Information

Desert locust-inspired wavelength-selective polarization vision by all two-dimensional ferroelectric heterostructures

Xiankai Lin,[1] Qian Zhang,[2,*] Wenbo Li,[1] Fang Yi,[3] Shihong Ma,[1] Guitian Qiu,[1] Jianxian Yi,[1,2] Jiwei Chen,[1] Yingjie Luo,[1] Chunlei Zhang,[1] Guigang Zhou,[1,2] Ziling Chen,[1] and Qijie Liang[1,*]

AFFILIATIONS

[1]*Songshan Lake Materials Laboratory, Songshan Lake Mat Lab, Dongguan 523808, China*

[2]*School of Materials, Shenzhen Campus of Sun Yat-sen University, No. 66, Gongchang Road, Guangming District, Shenzhen 518107, China*

[3]*School of Materials Science and Engineering, Sun Yat-sen University, Guangzhou, 510275 P. R. China*

[*]*E-mail: zhangqian6@mail.sysu.edu.cn; liangqijie@sslab.org.cn*

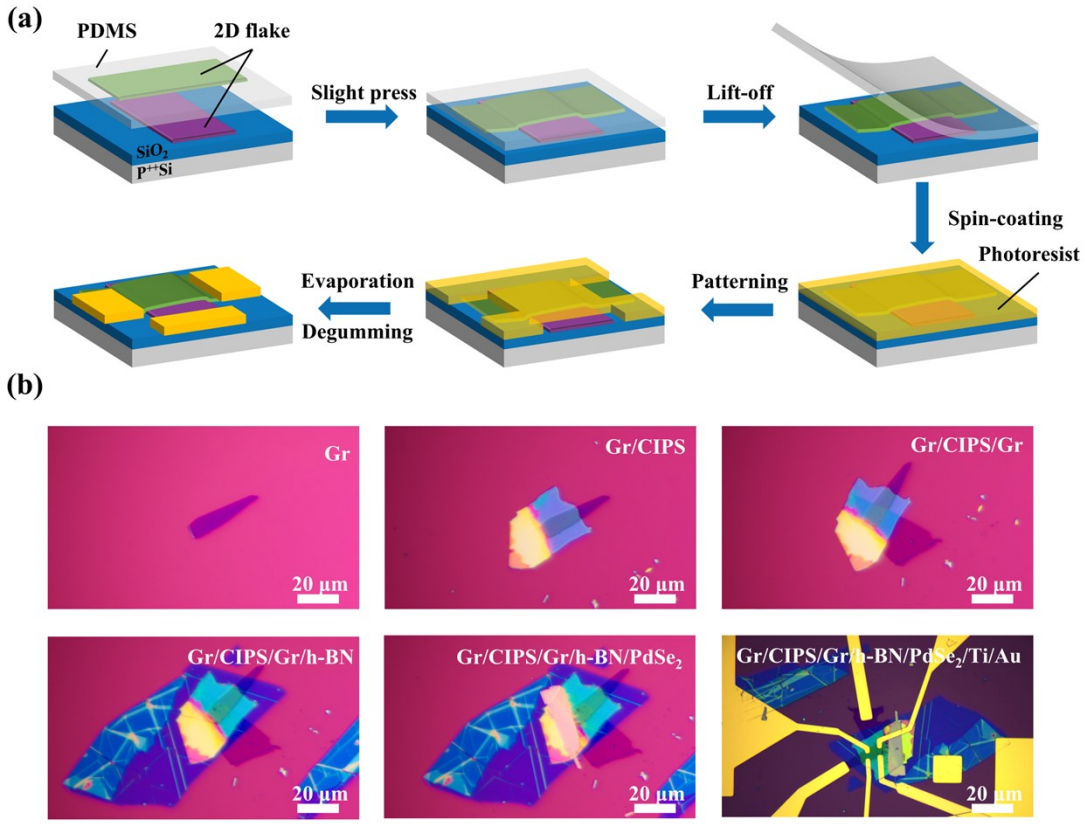

Figure S1. Fabrication process of the GCGhP ferroelectric heterostructure based BPVS. (a) Schematic of the fabrication process for the device structure. Using a PDMS-assisted transfer technique, a 2D flake was first transferred onto a $SiO_2/p^{++}Si$ substrate. A second flake was then aligned and transferred onto the pre-positioned flake through gentle pressing, followed by PDMS lift-off using a micromanipulator under an optical microscope, thereby forming the heterostructure. The process continued with spin-coating of photoresist, UV photolithography patterning, metal evaporation, and degumming, resulting in the final patterned device. (b) Optical microscope images of BPVS at different process stages.

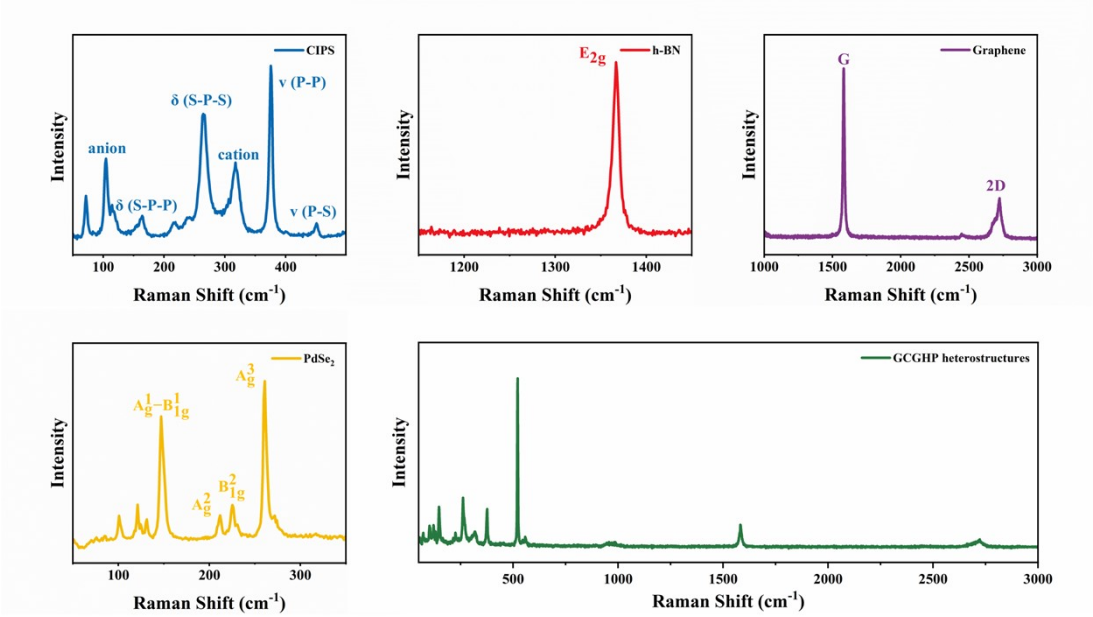

Figure S2. Raman spectra of $PdSe_2$, h-BN, Gr, CIPS, and GCGhP heterostructures. For $PdSe_2$ nanosheets, four distinct peaks were shown at 147.0, 211.9, 225.3, and 260.8 cm^{-1}. Correspond to the A_g^1 - B_{1g}^1、A_g^2、B_{1g}^2、A_g^3 mode. In addition, two distinct peaks appear at 100.8 and 121.1 cm^{-1}, indicating the low-layer nature of $PdSe_2$. For CIPS nanosheets, six vibrational peaks of activity modes were observed, including anion mode (104.4 cm^{-1}), δ (S-P-P) mode (164.0 cm^{-1}), δ (S-P-S) mode (264.4 cm^{-1}), cationic mode (317.4 cm^{-1}), ν (P-P) mode (375.6 cm^{-1}) and ν (P-S) mode (450.8) cm^{-1}). In contrast, the graphene nanosheets lacked D-peaks in their Raman spectra, which demonstrated their high-quality properties. In addition, the strength of the G-peak in the graphene sheet is much higher than that of the 2D peak, which indicates the multilayer nature of the graphene sheet. At the same time, h-BN exhibits Raman spectral characteristics similar to those previously reported[1].

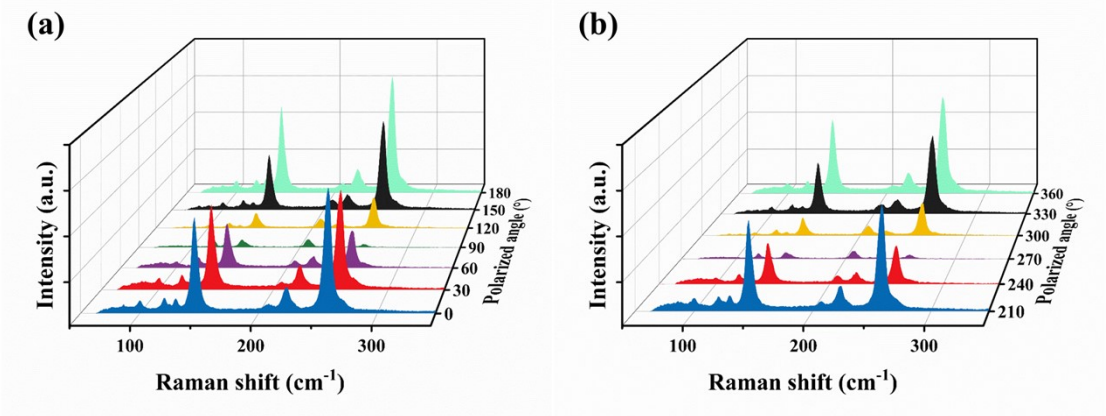

Figure S3. The angle-resolved polarized Raman spectroscopy measurements of the 2D $PdSe_2$ layer.

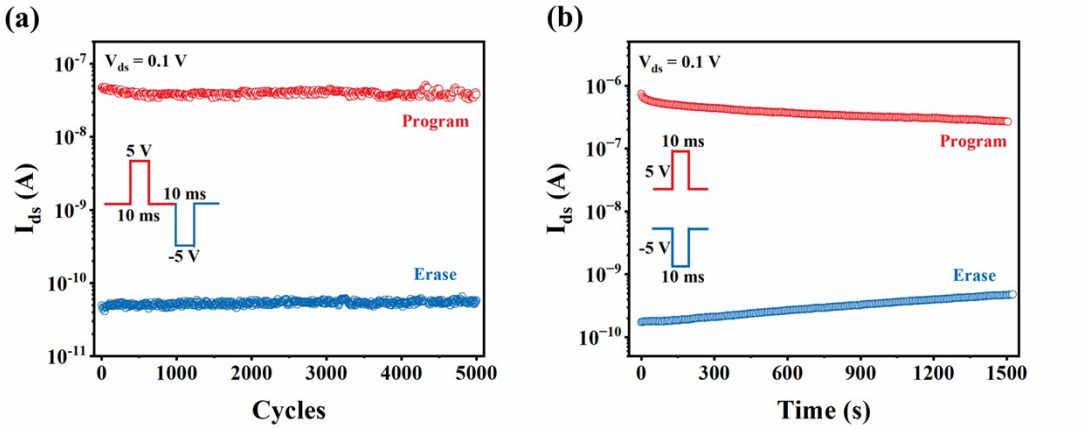

Figure S4. Non-volatile electronic memory behaviors of the BPVS. (a) Endurance performance through more than 5,000 Program/Erase cycles. (b) Retention stability through more than 1,500 s.

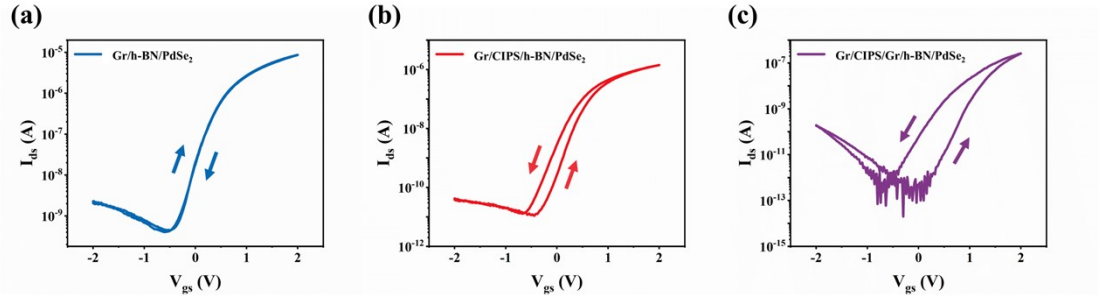

Figure S5. Transfer curves of $PdSe_2$-based transistors in different architectures. (a) The Gr/h-BN/$PdSe_2$ transistor has a hysteresis loop with a near-zero storage window, indicating a clean interface between h-BN and $PdSe_2$ nanosheets and a tiny charge-trapping effect at the interface. (b) The Gr/CIPS/h-BN/$PdSe_2$ transistor has a significant hysteresis window, indicating that the memory behavior of the BPVS originates from the ferroelectric medium, rather than the interface defect trapping of the channel and the dielectric. (c) The Gr/CIPS/Gr/h-BN/$PdSe_2$ transistor has a larger hysteresis window than the Gr/CIPS/h-BN/$PdSe_2$ transistor, due to compensation of upward and downward polarization in CIPS by Gr.

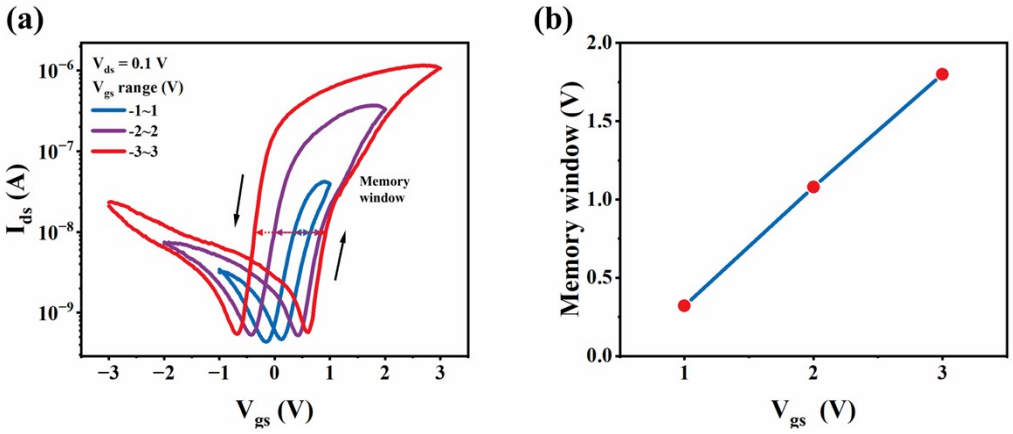

Figure S6. Electrical characteristics of BPVS under different V_{gs} scanning conditions. (a) Transfer characteristics measured at V_{ds} = 0.1 V with an increasing gate voltage sweep ranges (V_{gs}: ±1 V to ±3 V, step: 1 V). (b) The evolution of the memory window under different V_{gs} scanning ranges is extracted from (a).

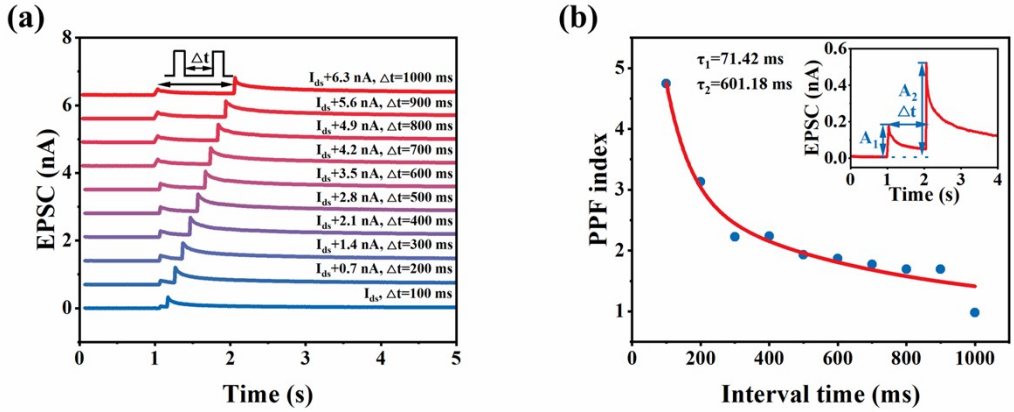

Figure S7. PPF behavior characterization of the BPVS. (a) Phenomenon of double pulse peaks was triggered by two consecutive electrical pulses (amplitude: 4 V, width: 10 μs) under different Δt. (b) PPF index values with respect to the interval of pulse pairs, where the red line is the fitted curve using the double exponential decay function.

When two consecutive electrical pulses at different time intervals (Δt) are applied to the device and the reading voltage is set to 0.5 V, the EPSC amplitude caused by the second electrical pulse is significantly larger than that by the first one, which is similar to the PPF behavior in biological synapses. The PPF index is defined as

$$\text{PPF index} = \frac{(A_2 - A_1)}{A_1} \times 100\% \#(1)$$

Where, A_1 and A_2 represent the first and second peaks of EPSC, respectively. It is worth noting that as Δt increases from 100 ms to 1000 ms, the PPF index decreases from 500% to 100%.

As Δt increased, the PPF index exhibits a declining trend, which can be fitted using a double-exponential function:[2]

$$\text{PPF index} = 1 + C_1 e^{\left(\frac{-\Delta t}{\tau_1}\right)} + C_2 e^{\left(\frac{-\Delta t}{\tau_2}\right)} \#(2)$$

Where, C_1 and C_2 represent initial facilitation values respectively, and $\tau_1 = 71.42$ ms and $\tau_2 = 601.18$ ms represent fast decay time and slow decay time, respectively. The fitting results are comparable to those of biological synapses.[3]

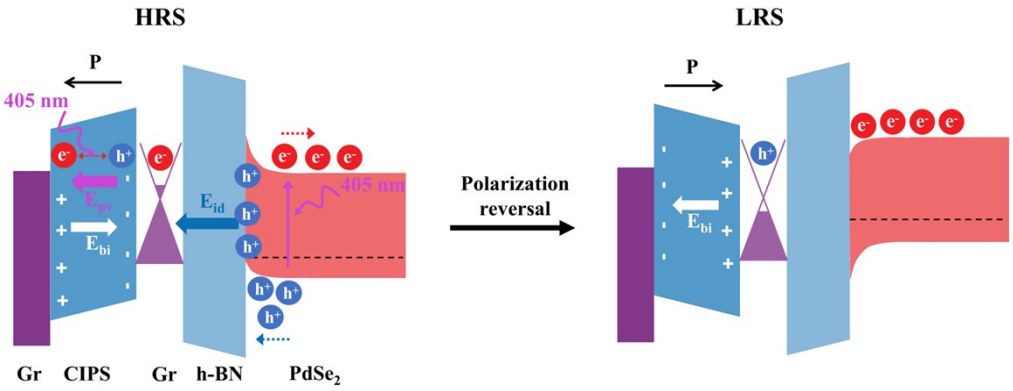

Figure S8. Schematic diagram of short-term memory characteristics induced by photovoltaic electric field (E_{pv}) and induced electric field (E_{id}) collaborate.

In the initial stage, a negative voltage pulse is applied to the gate, driving the transistor into a high resistance state (HRS). Subsequently, upon ultraviolet light irradiation, a large number of electron-hole pairs are generated within $PdSe_2$. At this juncture, holes accumulate at the $PdSe_2$/h-BN interface, inducing electron doping in graphene and generating an induced electric field within the heterostructure. Moreover, considering that CIPS is a non-centrosymmetric crystal, under ultraviolet light illumination, the momentum of photogenerated carriers exhibits an asymmetric distribution. This asymmetry leads to the generation of a E_{pv} within CIPS, which is opposite in direction

to the built-in electric field (E_{bi}).[4] Ultimately, under the combined influence of E_{pv} and E_{id}, the polarization of CIPS is reversed. Consequently, the transistor transitions from a HRS to a low resistance state (LRS), and this LRS can be sustained for a short duration.

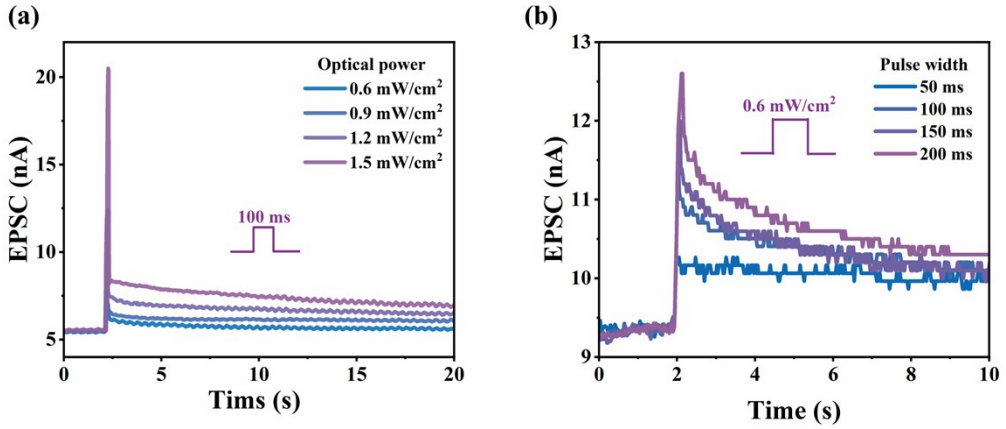

Figure S9. Characterization of optical synaptic plasticity. Photocurrent responses trigged by single optical pulse with different (a) power densities and (b) pulse width, respectively.

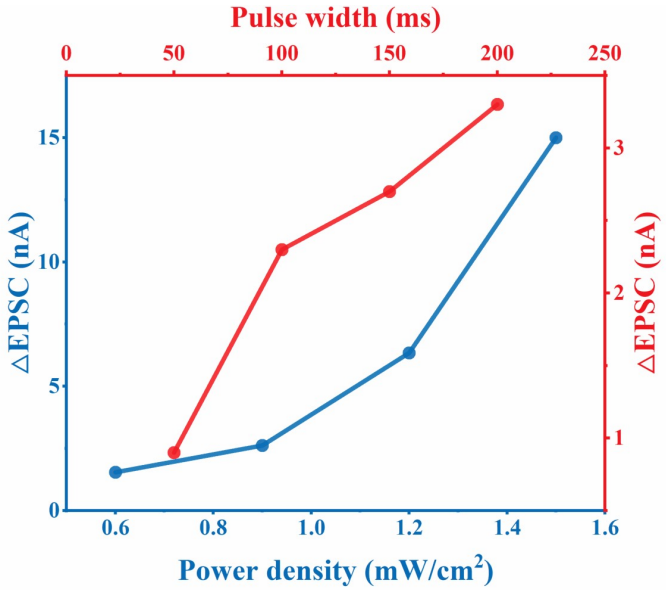

Figure S10. The modulation of EPSC by optical power and pulse width.

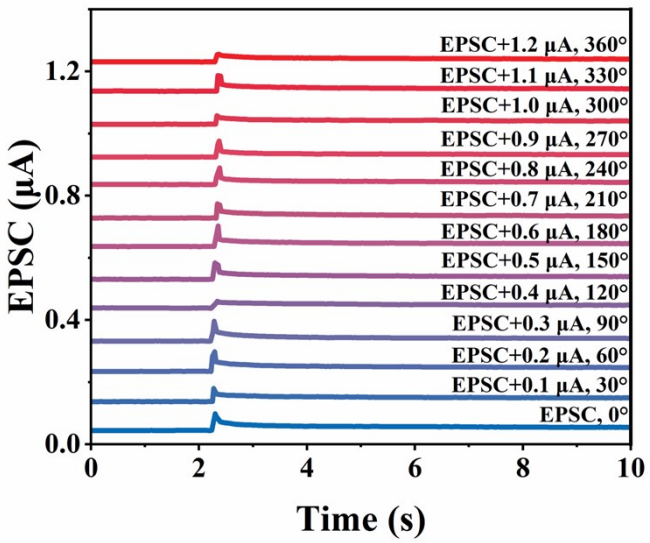

Figure S11. EPSC trigged by single optical pulse (intensity: 0.9 mW/cm^2，width: 100 ms) with different polarization angles.

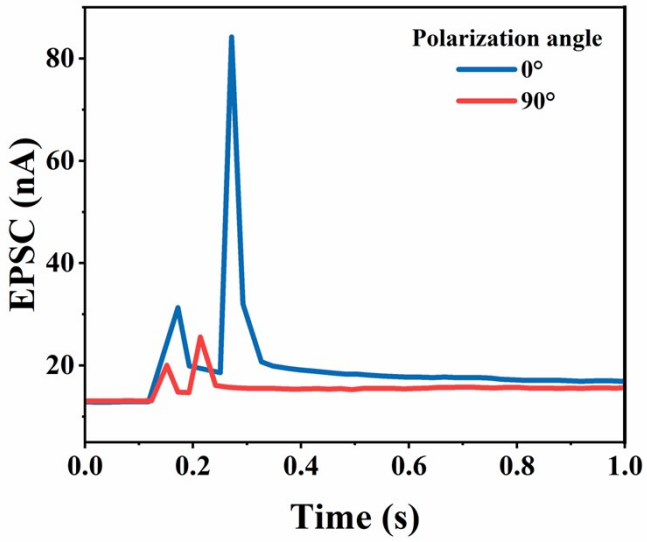

Figure S12. Phenomenon of double pulse peaks triggered by two consecutive optical pulses (intensity: 0.9 mW/cm^2, width: 100 ms, interval: 100 ms) at 0° and 90° polarization angles, respectively.

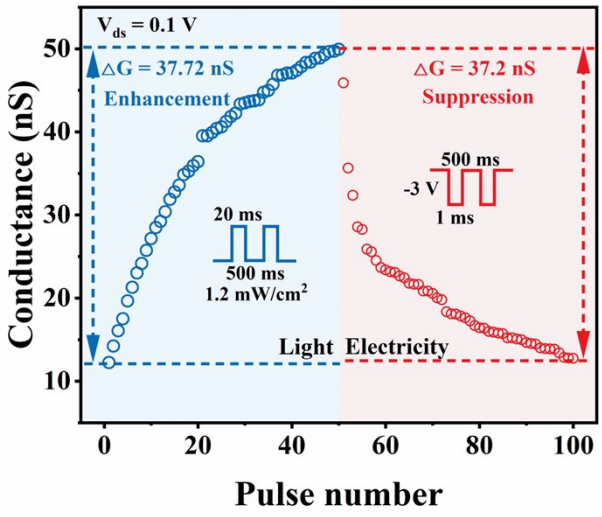

Figure S13. The enhancement and suppression properties triggered by optical pulses and electrical pulses.

The average energy expenditure of a neuromorphic system during its training and learning can be calculated using the following formula:

$$E_{ave} = \frac{\left(V_{ds}^{\ 2} \times \Delta G \times \Delta t\right)}{N}$$

Where V_{ds} is the training voltage, ΔG is the delta value of conductance before and after training, Δt is the width of the training pulse and N is the number of pulses. The calculated energy consumption of BPVS in enhancement (0.15 pJ per spike) and suppression (7.44 fJ per spike).

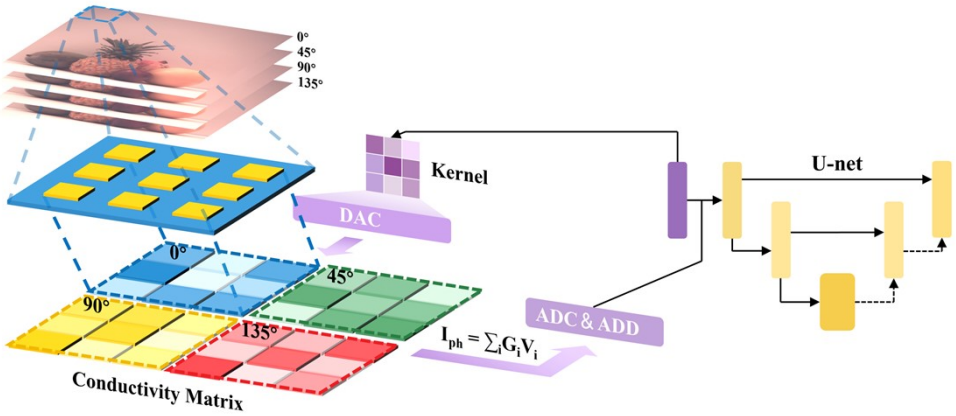

Figure S14. Flow chart of polarization images convolution operation based on a 3×3 BPVS array.

In the polarization image reconstruction, a 3×3 convolution kernel is utilized, which corresponds to the first convolution layer of the U-net model. The convolution kernel accomplishes image local - feature extraction via a 2D discrete convolution operation, and its functional matrix can be expressed as:

$$W = [[w_{11}, w_{12}, w_{13}], [w_{21}, w_{22}, w_{23}], [w_{31}, w_{32}, w_{33}]]$$

where w_{ij} represents trainable weight parameters, which are optimized by gradient descent algorithm. At the hardware implementation level, the normalized weight parameters are transformed into an analog voltage signal V_{ds} by a high-precision digital -to-analog converter (DAC) and then loaded onto a 3×3 BPVS array. The conductivity state of each BPVS unit corresponds to the pixel value of the input image. Images with different polarization angles are successively mapped from “pixel value- conductance value” to achieve 36-level (6-bit) discrete conductivity state quantization. Next, the BPVS array accomplishes the convolution operation through the channel current modulation of the van der Waals heterojunction. When V_{ds} is applied to the 3×3 BPVS array, the current output of each BPVS unit is $I_{ph} = G_i \cdot V_i$ (where G_i is the device conductance). The convolution result is obtained after summation by an integrating circuit, obviating the pixel-by-pixel multiplication-summation (MAC) operation of a traditional digital circuit.[5]

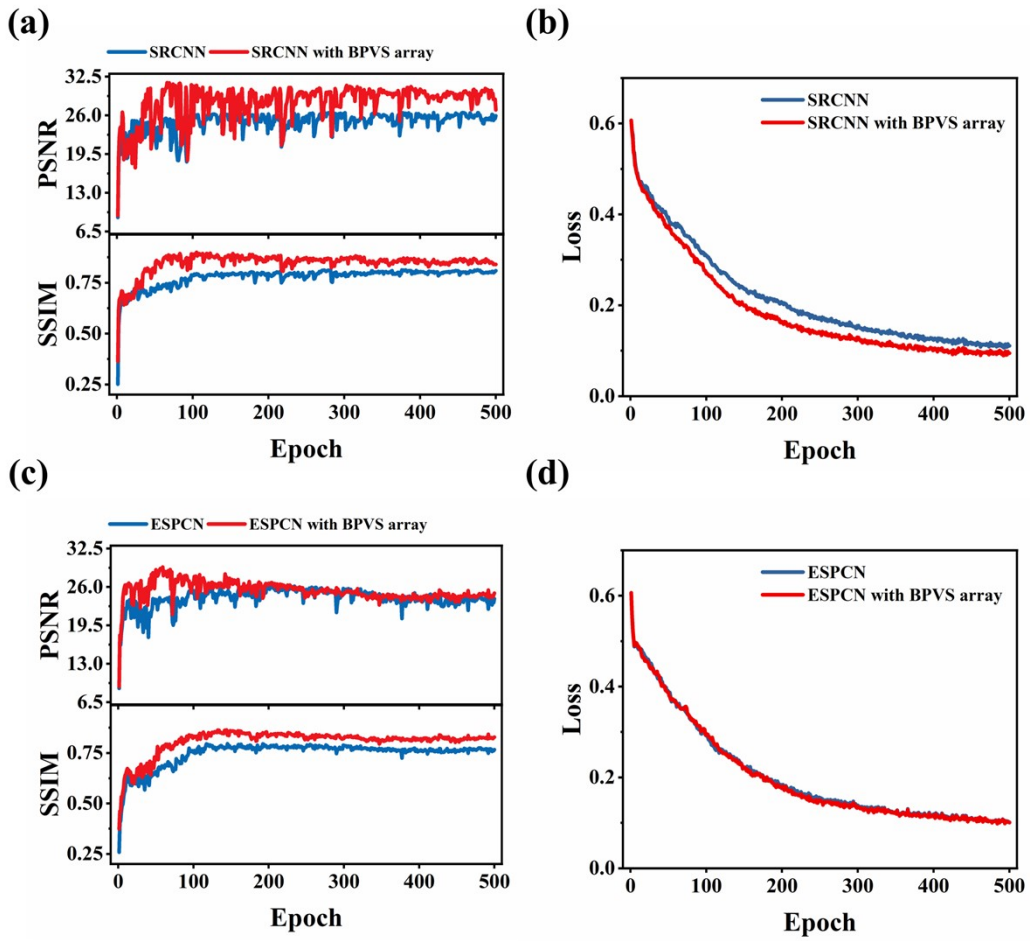

Figure S15. Comparative evaluation of SR reconstruction performance. (a, b) PSNR, SSIM, and loss values for polarization images reconstructed by the SRCNN model with and without the BPVS array, respectively. (c, d) PSNR, SSIM, and loss values for the ESPCN model with and without the BPVS array, respectively.

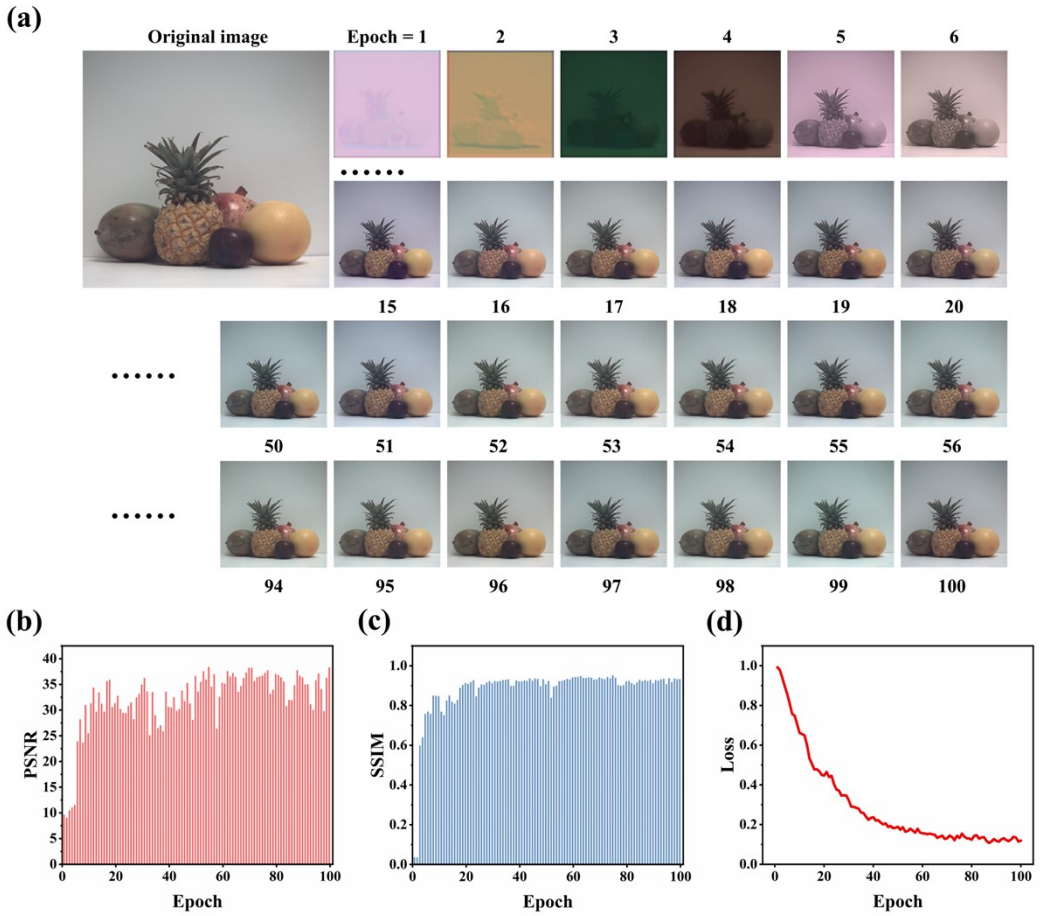

Figure S16. Demonstration of SR reconstruction of color polarization images with increasing iterations based on UBPVS-net architecture. (a) Visual results from the first to the 100th training cycle. (b-d) PSNR, SSIM and loss values were calculated based on reconstructed polarization images from the first to the 100th training cycle.

The both PSNR and SSIM plateau after approximately 20 epochs, indicating that the model had effectively completed learning the global image features such as structure, luminance, and contrast. Beyond this stage, the model continued to refine subtle pixel-level deviations, with the loss continuing to decline gradually until full convergence. It should be noted that PSNR is derived from a logarithmic transformation of the mean square error (MSE) ($PSNR = 10log_{10}\left(\frac{n^2}{MSE}\right)$, n is defined as the total pixel count). As a result, even minor variations in MSE can lead to noticeable fluctuations in PSNR values, which explains the pronounced PSNR fluctuations observed during the training stages.

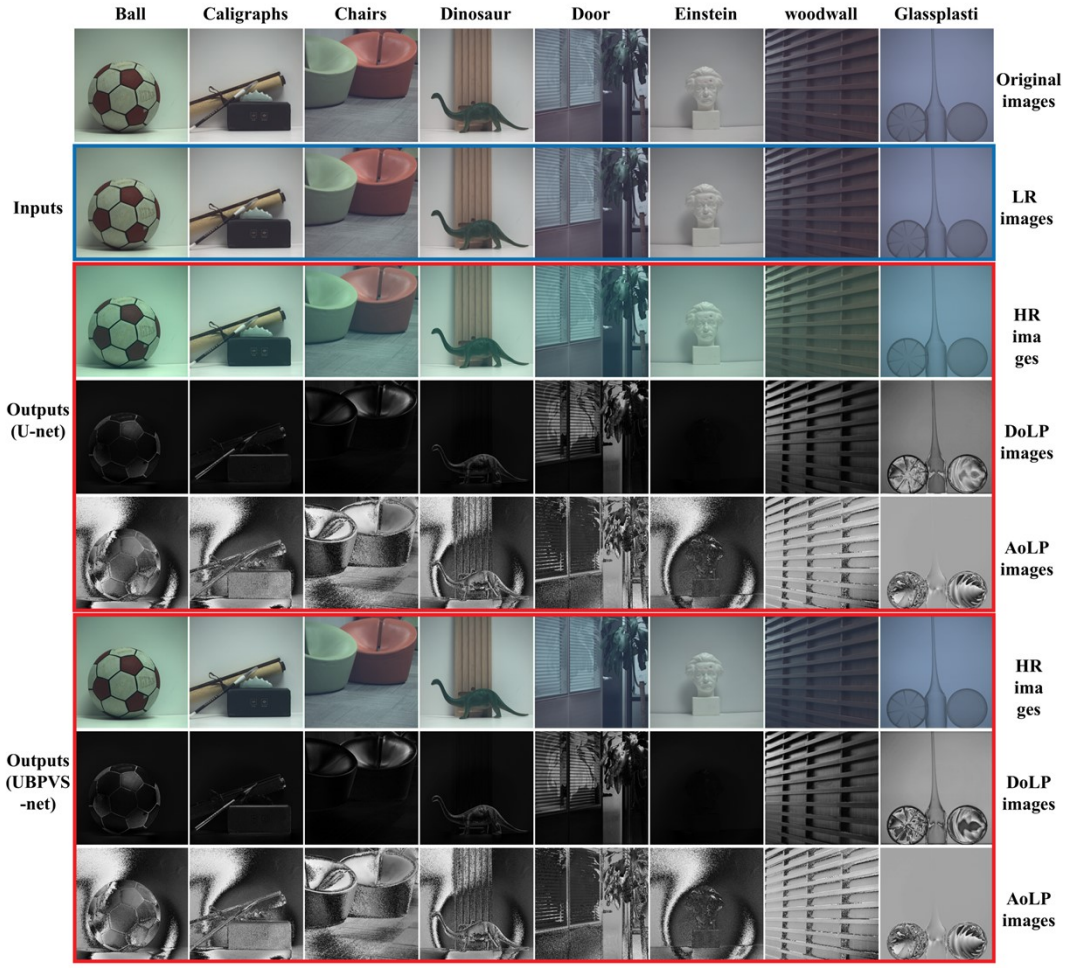

Figure S17. Demonstration of SR reconstruction of multiple color polarization images based on UBPVS-net and U-net architectures.

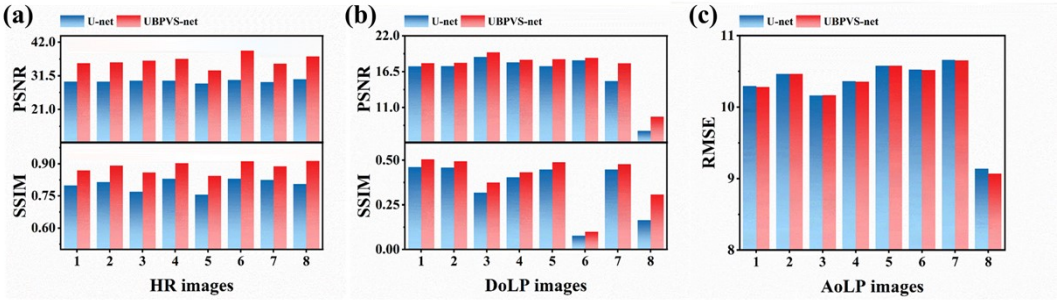

Figure S18. Evaluation indices of reconstructed multiple color polarization images UBPVS-net and U-net architectures. (a, b) PSNR and SSIM values were calculated from the reconstructed HR images and DoLP images. (c) The RMSE values were calculated from the reconstructed AoLP images. The numbers 1, 2, 3, 4, 5, 6, 7, and 8

represent the ball, calligraphset, chairs, dinosaur, door, Einstein, woodwall, and glassplastic, respectively.

Table S1. Comparison of the structure and performance of other types of 2D ferroelectric devices.

Configuration	Structure	Cycle Endurability	Electronic Retention	Electronic LTP/LTD Endurability	Ref.
Two-terminal	Gr/α-In_2Se_3/Gr	-	-	3 cycles, 400 pulse numbers	6
Two-terminal	Ti/α-In_2Se_3/Au	>100	>5000 s	-	7
Three-terminal	Si/SiO_2/SnSe/Ti/Au	~50	>3600 s	4 cycles, 250 pulse numbers	8
Three-terminal	IGZO/SnO/SnS	-	-	8 cycles, 650 pulse numbers	9
Two-terminal	Au/CIPS/Gr	-	-	10 cycles, 400 pulse numbers	10
Two-terminal	Au/CIPS/MoS_2/Gr	-	-	-	11
Three-terminal	Au/CIPS/h-BN/ReS_2	-	>1000 s	-	4
Three-terminal	Au/CIPS/MoS_2	-	-	-	12
Four-terminal	Au/CIPS/h-BN/WSe_2	-	-	-	13
Two-terminal	Au/CIPS/Ti	>100	>2000 s	-	14
Three-terminal	Gr/CIPS/Gr/h-BN/$PdSe_2$	>5000	>1500 s	90 cycles, 9000 pulse numbers	This work

Table S2. Comparison of the structure and performance of other types of bionic polarization visual devices.

Structure	Mechanism	Polarization type	On/Off	Wavelength	Synaptic plasticity	Network	Ref.
H-PVKs/SWNTs	Defects capture	Circular	-	395 nm to 470 nm	EPSC, PPF, STP, LTP and SEDP	SNN (MNIST)	15
Cl_2-NDI/PBI-1	Defects capture	Linear	$>10^4$	414 nm, 645 nm	EPSC, IPSC and STDP	-	16
3D Gr/MoS_2	Defects capture	Linear	$\sim10^3$	365 nm to 808 nm	IPSC, PPF, STD, and LTD	-	17
ReS_2	Defects capture	Linear	$>10^3$	552 nm, 860 nm	EPSC, STDP and SEDP	-	18
UiO-66-NH_2 /ReS_2	Defects capture	Linear	$>10^3$	552 nm, 860 nm	EPSC	-	19
PbS QDs/Gr	Defects capture	Linear	-	405 nm	EPSC, IPSC, LTP, and LTD	ANNs (MNIST)	20
C8-BTBT	Defects capture	Linear	-	365 nm, 525 nm	-	-	21
ReS_2/$GeSe_2$	Defects capture	Linear	$\sim10^2$	405 nm, 808 nm	EPSC, IPSC, LTP, and LTD	ANNs	22
Gr/CIPS/Gr/h-BN/$PdSe_2$	Ferroelectric polarization	Linear	$>10^3$	405 nm	EPSC, PPF, STP, LTP, LTD, and SEDP	UBPVS-net (Ploarization images SR reconstruction)	This work

1

2 References

3 1 J. Zha, S. Shi, A. Chaturvedi, H. Huang, P. Yang, Y. Yao, S. Li, Y. Xia, Z. Zhang,
4 W. Wang, H. Wang, S. Wang, Z. Yuan, Z. Yang, Q. He, H. Tai, E. H. T. Teo, H.
5 Yu, J. C. Ho, Z. Wang, H. Zhang and C. Tan, *Adv. Mater.*, 2023, **35**, 2211598.
6 2 S. M. Kwon, S. W. Cho, M. Kim, J. S. Heo, Y. Kim and S. K. Park, *Adv. Mater.*,

2019, **31**, 1906433.

3 R. S. Zucker and W. G. Regehr, *Annu. Rev. Physiol.*, 2002, **64**, 355–405.

4 M. Soliman, K. Maity, A. Gloppe, A. Mahmoudi, A. Ouerghi, B. Doudin, B. Kundys and J.-F. Dayen, *ACS Appl. Mater. Interfaces*, 2023, **15**, 15732–15744.

5 Y. Xia, N. Lin, J. Zha, H. Huang, Y. Zhang, H. Liu, J. Tong, S. Xu, P. Yang, H. Wang, L. Zheng, Z. Zhang, Z. Yang, Y. Chen, H. P. Chan, Z. Wang and C. Tan, *Adv. Mater.*, 2024, **36**, 2403785.

6 J. Zeng, G. Feng, G. Wu, J. Liu, Q. Zhao, H. Wang, S. Wu, X. Wang, Y. Chen, S. Han, B. Tian, C. Duan, T. Lin, J. Ge, H. Shen, X. Meng, J. Chu and J. Wang, *Adv. Funct. Mater.*, 2024, **34**, 2313010.

7 Y. Zhang, L. Wang, H. Chen, T. Ma, X. Lu and K. P. Loh, *Adv. Elect. Mater.*, 2021, **7**, 2100609.

8 Z. Liu, Y. Wang, Y. Zhang, S. Sun, T. Zhang, Y. Zeng, L. Hu, F. Zhuge, B. Lu, X. Pan and Z. Ye, *Adv. Mater.*, 2025, **37**, 2410783.

9 R. Yang, D. Hu, Q. Chen, Z. Wang, B. Lu, Z. Ye, X. Li and J. Lu, *Adv. Funct. Mater.*, 2025, **35**, 2414210.

10 Y. Liu, Y. Wu, H. Han, Y. Wang, R. Peng, K. Liu, D. Yi, C. Nan and J. Ma, *Adv. Funct. Mater.*, 2024, **34**, 2306945.

11 Z. Wang, J. Li, X. Fan, W. Tang, H. Zhu and L. Li, *Adv. Mater. Tech.*, 2024, 2401589.

12 X. Wang, P. Yu, Z. Lei, C. Zhu, X. Cao, F. Liu, L. You, Q. Zeng, Y. Deng, C. Zhu, J. Zhou, Q. Fu, J. Wang, Y. Huang and Z. Liu, *Nat. Commun.*, 2019, **10**, 3037.

13 A. Ram, K. Maity, C. Marchand, A. Mahmoudi, A. R. Kshirsagar, M. Soliman, T. Taniguchi, K. Watanabe, B. Doudin, A. Ouerghi, S. Reichardt, I. O'Connor and J.-F. Dayen, *ACS Nano*, 2023, **17**, 21865–21877.

14 B. Li, S. Li, H. Wang, L. Chen, L. Liu, X. Feng, Y. Li, J. Chen, X. Gong and K. Ang, *Adv. Elect. Mater.*, 2020, **6**, 2000760.

15 Q. Liu, Q. Wei, H. Ren, L. Zhou, Y. Zhou, P. Wang, C. Wang, J. Yin and M. Li, *Nat. Commun.*, 2023, **14**, 7179.

16 J. H. Kim, M. Stolte and F. Würthner, *ACS Nano*, 2022, **16**, 19523–19532.

17 Y. Li, Y. Zhang, Y. Wang, J. Sun, Q. You, M. Zhu, L. Li and T. Deng, *Adv. Funct. Mater.*, 2024, **34**, 2302288.

18 D. Xie, K. Yin, Z.-J. Yang, H. Huang, X. Li, Z. Shu, H. Duan, J. He and J. Jiang, *Mater. Horiz.*, 2022, **9**, 1448–1459.

19 D. Xie, G. Gao, B. Tian, Z. Shu, H. Duan, W. Zhao, J. He and J. Jiang, *Adv. Mater.*, 2023, **35**, 2212118.

20 K.-J. Lee, J. H. Kim, S. Jeon, C. W. Shin, H.-R. Kim, H.-G. Park and J. Kim, *Nano Lett.*, 2024, **24**, 2421–2427.

21 J. Pan, Y. Wu, X. Zhang, J. Chen, J. Wang, S. Cheng, X. Wu, X. Zhang and J. Jie, *Nat. Commun.*, 2022, **13**, 6629.

22 T. Guo, S. Li, Y. N. Zhou, W. D. Lu, Y. Yan and Y. A. Wu, *Nat. Commun.*, 2024, **15**, 6731.